

1 A simultaneous observation of lightning by ASIM,  
2 Colombia-Lightning Mapping Array, GLM and ISS-LIS

3

4 Joan Montanyà<sup>1</sup>, Jesús A. López<sup>1</sup>, Carlos A. Morales Rodriguez<sup>2</sup>, Oscar A.  
5 van der Velde<sup>1</sup>, Ferran Fabró<sup>3,1</sup>, Nicolau Pineda<sup>3,1</sup>, Javier Navarro-  
6 González<sup>4</sup>, Víctor Reglero<sup>4</sup>, Torsten Neubert<sup>5</sup>, Olivier Chanrion<sup>5</sup>, Steven J.  
7 Goodman<sup>6</sup>, Nikolai Østgaard<sup>7</sup>, Alfonso Ladino-Rincon<sup>8</sup>, David Romero<sup>1</sup>,  
8 Glòria Solà<sup>1</sup>, Ricard Horta<sup>1</sup> and Modesto Freijó<sup>1</sup>

9

- 10 1. Lightning Research Group, Dept. of Electrical Engineering, Polytechnic University of Catalonia  
11 (UPC), Colom 1, 08222 Terrassa (Barcelona), Spain
- 12 2. Departamento de Ciências Atmosféricas, Instituto de Astronomia, Geofísica e Ciências Atmosféricas,  
13 Universidade de São Paulo, São Paulo, Brazil
- 14 3. Meteorological Service of Catalonia, Barcelona, Spain
- 15 4. Image Processing Laboratory, University of Valencia, Valencia, Spain
- 16 5. National Space Institute, Technical University of Denmark, (DTU-Space), Elektrovej Bld. 328, 2800  
17 Kgs. Lyngby, Denmark
- 18 6. Thunderbolt Global Analytics, Owens Cross Roads, AL USA
- 19 7. Birkeland Centre for Space Science, Dept. of Physics and Technology, University of Bergen, Bergen,  
20 Norway
- 21 8. Department of Atmospheric Sciences, University of Illinois, Urbana, IL USA

22

23 Key points:

24

- 25 1. Features of luminosity from a lightning flash detected by ASIM, GLM and LIS  
26 are related with leader development and cloud properties.
- 27 2. Surges in 777.4 nm luminosity are associated with return stroke currents,  
28 continuing currents, recoil leaders and leader branching.
- 29 3. Altitude of lightning leaders, cloud particles above lightning channels as well as  
30 channel luminosity influence the detection of light.

31

32

33

34

35

36

37

38 **Abstract**

39

40 The Atmosphere-Space Interactions Monitor (ASIM) on the International Space Station  
41 (ISS) provides optical radiances and images of lightning flashes in several spectral bands.  
42 This work presents a lightning flash simultaneously observed from space by ASIM, the  
43 Geostationary Lightning Mapper (GLM) and the Lightning Imaging Sensor on the  
44 International Space Station (ISS-LIS); and from ground by the Colombia Lightning  
45 Mapping Array (Colombia-LMA). Volumetric weather radar provides reflectivity data to  
46 help to interpret the effects of the cloud particles on the observed optical features. We  
47 found that surges in radiance in the band at 777.4 nm appear to be related mostly with  
48 lightning processes involving currents as well with branching of lightning leaders with  
49 new leader development. In cloud areas with reflectivity <18 dBZ above the lightning  
50 leader channels at altitudes >7 km, these have been imaged by ASIM and GLM. But in  
51 the region with reflectivity <23 dBZ, despite its lower cloud tops and similar altitudes of  
52 lightning channels, these have been almost undetectable. The calculated relative optical  
53 depths are consistent with the observed optical intensity at the cloud top. Despite the  
54 effects of the cloud particles and the altitude of the lightning channels on the attenuation  
55 of the luminosity, the luminosity of the lightning channels due to different processes is  
56 fundamental for the imaging of lightning from space.

57

58 **1. Introduction**

59

60 In the near future, much of the Earth's lightning activity will be continuously monitored  
61 from space by lightning imagers placed in geostationary orbit. These new satellite-based  
62 instruments open a new era of weather monitoring and research into the role of  
63 thunderstorm processes in the dynamics of the atmosphere and in climate change. The  
64 Geostationary Lightning Mapper (GLM) on the first of the Geostationary Operational  
65 Environmental Satellite GOES-R Series (GOES-16 at 75.2W) is the first lightning  
66 detector in geostationary orbit (*Goodman et al.*, 2013; *Rudlosky et al.*, 2019ab). GLM is  
67 based on its predecessors, the Optical Transient Detector (OTD) and Lightning Imaging  
68 Sensor (LIS) (*Christian et al.*, 1989). In China, the Lightning Mapping Imager (LMI) on  
69 the Feng-Yun4 is detecting lightning in Asia (*Yang et al.*, 2017) and in the near future,  
70 Europe and Africa will be continuously monitored by the Lightning Imager (LI) on the

71 Meteorol Third Generation satellites (MTG) (*Stuhlmann et al., 2005*). All of these  
72 systems, new to the geostationary orbit, use optical imagers at the narrow spectral line at  
73 the 777.4 nm infrared emission of atomic oxygen that is associated with hot lightning  
74 channels (e.g. *Soler et al., 2020*).

75 The Atmosphere-Space Interactions Monitor (ASIM) on the International Space Station  
76 (ISS) consists of a suite of optical instruments and X- and gamma-ray detectors for  
77 investigating lightning, Transient Luminous Events (TLEs) and Terrestrial Gamma-ray  
78 Flashes (TGFs) (e.g. *Chanrion et al., 2019; Neubert et al., 2019*). ASIM is equipped with  
79 three photometers at 180-230 nm, 337.0 nm and 777.4 nm spectral bands plus two one-  
80 megapixel cameras at 337.0 nm and 777.4 nm. The objective of the 337.0 nm (blue) and  
81 777.4 nm (red) instruments is to quantify optical energy leaving from the top of the clouds  
82 and to provide images of lightning events. The selected red (777.4 nm) band monitors the  
83 emission from neutral atomic oxygen caused by lightning processes like the return stroke  
84 and recoil leader events (e.g. *Thomas et al., 2000*) whereas the blue (337.0 nm) emissions  
85 are characteristic of the N<sub>2</sub> 2<sup>nd</sup> positive system (SPS) which are common in electrical  
86 discharges but have been little investigated in lightning. Recently, *Soler et al. (2020)* have  
87 shown blue optical emissions with absence of red to be related with narrow-bipolar  
88 events. In these cases, the blue emission is considered to be produced by cold electrical  
89 discharges like streamers. In addition to the red and blue channels, the selected far UV  
90 (180-230 nm) channel allows the discrimination of TLEs in the higher atmosphere since  
91 the optical emissions in this band coming from the troposphere (e.g. from lightning)  
92 would be highly attenuated. Because ASIM instruments provide high temporal and spatial  
93 resolution of optical activity in the clouds with additional spectral bands. ASIM offers an  
94 opportunity to explore in more detail the performance of the lightning imagers in  
95 geostationary orbit (e.g. *van der Velde et al., 2020*). The comparison of data from ASIM  
96 in the low-Earth-orbit of the ISS (~400 km, 51.6° inclination) to the geostationary  
97 instruments is facilitated by a LIS instrument, also on the ISS (*Blakeslee et al., 2020*).

98

99 The optical emission from lightning that escapes from a cloud is highly affected by  
100 scattering and absorption of photons by cloud particles which reduce the signal intensity,  
101 and broadens emissions in space and time (e.g. *Thomason and Krider, 1982; Peterson,*  
102 *2019; Thomason and Krider, 1982; Koshak et al., 1994; Light et al., 2001; Peterson, 2014;*  
103 *Luque et al., 2020; Brunner and Bitzer, 2020*). This effect has been the subject of several  
104 studies that compare detection from space with data from lightning detection systems at

105 ground. In particular, the measurements of Lightning Mapping Array (LMA) networks  
106 (*Rison et al., 1999*) have been useful because they provide 3D reconstructions of lightning  
107 leader development inside the clouds. The early comparisons between LIS and LMA  
108 (*Thomas et al., 2000*) showed that most of the detected optical events were associated  
109 with lightning channels at the upper part of the storms. Cloud-to-ground (CG) flashes  
110 confined to mid and lower altitudes were less detected. In addition, the strongest light  
111 emissions were identified to be related with impulsive high current events from recoil  
112 leader activity. Most of the works comparing space-based optical detections and LMA  
113 flash data focused on the evaluation of the detection efficiency (e.g. *Montanyà et al. 2019*;  
114 *Erdmann et al., 2020*; *Zhang and Cummins, 2020*). In these works, only lightning is  
115 considered but not the microphysical characteristics of the clouds in which lightning  
116 flashes are immersed and their effect on to the propagation of light. Recently, *Rutledge et*  
117 *al. (2020)* has incorporated radar and LMA data to evaluate GLM. In this work it has been  
118 identified that GLM detection efficiency depends on the lightning flash geometric size,  
119 in agreement with *Zhang and Cummins (2020)*, and the cloud water path. The size of the  
120 flash was found to be correlated with the optical brightness whereas the cloud water path  
121 was related to the optical extinction. The cloud water path, in turn, depends on the height  
122 of the flash that was derived from LMA clustered data and the cloud water content. Using  
123 radar, the mean precipitation-sized hydrometeor ice water paths were determined but,  
124 with S-band radars, cloud particles cannot be detected. The authors pointed out that  
125 despite the small surface areas of cloud particles compared to precipitation-sized ones,  
126 their greater concentrations can provide more attenuation of optical energy. In the present  
127 work we complement the previously introduced works by relating lightning processes and  
128 cloud properties in a LMA flash case observed with the high resolution ASIM  
129 photometers and cameras.

130

131 This study presents the first report of a lightning flash occurring in a location with  
132 simultaneous coverage by the optical photometers and cameras of ASIM, the Colombia-  
133 LMA, the GOES-16 Advanced Baseline Imager (ABI), weather radar data, the GLM and  
134 the ISS-LIS. The flash occurred on November 22, 2018 at 08:57:21.4413 UT. We analyze  
135 the measurements of the ASIM, GLM and ISS-LIS instruments relative to the lightning  
136 propagation detected by the LMA and the influence of cloud properties estimated from  
137 weather radar data. The object of the analysis is to identify the relation of the red and blue

138 optical emissions with different lightning processes and the effects of the cloud properties  
139 on the measured luminosity.

140

141

## 142 **2. Data**

143

144 As ground support for the ASIM mission, the group at the Polytechnic University of  
145 Catalonia (UPC) installed one LMA in the Ebro river delta in North-Eastern Spain and  
146 another in Colombia (*van der Velde and Montanyà, 2013; López et al., 2019*). At the time  
147 of the event, the Colombia-LMA was composed of 6 stations close to the city of  
148 Barrancabermeja ( $\sim 7^{\circ}\text{N}$ ,  $73.85^{\circ}\text{W}$ ) in Colombia. The LMA system detects sources of  
149 radio emissions in the very high frequency range (VHF, 30-300 MHz) that originate from  
150 the breakdown processes related to the propagation of lightning leaders. The sources are  
151 located in three dimensions using the time-of-arrival technique. Detailed information  
152 about the LMA can be found in *Rison et al. (1999)* and *Thomas et al. (2004)*.

153

154 The Modular Multispectral Imaging Array (MMIA) optical sensors of ASIM are three  
155 photometers at 180-230 nm (UV), 337.0 nm (4 nm bandwidth) (hereafter the blue signal)  
156 and 777.4 nm (5 nm bandwidth) (hereafter the red signal) at 10 microsecond resolution,  
157 and two cameras with 1000 x1000 pixels and 12 frames per second at 337.0 nm (5 nm  
158 bandwidth) and 777.4 nm (3 nm bandwidth). The angle of view of the blue and red  
159 photometers is  $80^{\circ}$  with a square sensor. The UV photometer has a circular sensor with  
160 an angle of view of  $80^{\circ}$ . The spatial resolution of the cameras is  $\sim 400$  m per pixel towards  
161 nadir. A more detailed description of the instruments is found in *Chanrion et al. (2019)*  
162 and in *van der Velde et al. (2020)*.

163

164 The Geostationary Lightning Mapper (GLM) and the Lightning Imaging Sensor (ISS-  
165 LIS) provide locations of the sources (events) of luminosity for the investigated lightning  
166 flash with 2 ms resolution (*GOES-R Algorithm Working Group and GOES-R Series  
167 Program, 2018*). The minimum pixel footprints of GLM and ISS-LIS imagers are 8 km  
168 and 4 km, respectively. Radiance at the measured 777.4 nm narrow band for each event  
169 is provided.

170

171 Cloud-to-ground (CG) lightning locations and peak currents are provided by the  
172 Keraunos SAS LINET type lightning network in Colombia (Betz *et al.*, 2009; Aranguren  
173 *et al.*, 2017) and by the World-Wide Lightning Location Network (WWLLN, e.g. Rodger  
174 *et al.*, 2006). Additionally, extremely low frequency (ELF) magnetic fields (<0.01 to 300  
175 Hz) measured by the UPC Schumann resonance station in Cape Verde (16.73°N,  
176 22.93°W) are used to identify the presence of continuing currents for those transient  
177 events superimposed over the continuous Schumann resonance background (e.g.  
178 Boccippio *et al.*, 1995; Burke and Jones, 1996; Huang *et al.*, 1999).

179

180 Finally, radar reflectivity (Z) products are provided by the dual polarization C-band  
181 Doppler weather radar located in Barrancabermeja of the Colombian Instituto de  
182 Hidrología, Meteorología y Estudios Ambientales (IDEAM). It makes volumetric  
183 measurements every 8 minutes with 6 elevations and a gate resolution of 100 meters  
184 Cáceres (2017). Although the radar scan strategy was configured to sample the  
185 precipitation, the highest 2 elevations were able to measure heights from 8 to 17 km for  
186 distances from 30 to 67 km where the investigated flash occurred. The derived products  
187 used in this study are the maximum Z ( $Z_{\max}$ ), which corresponds to the maximum Z  
188 observed in the column at the gate position, and the contoured-frequency-altitude diagram  
189 (CFAD) of Z along the corresponding locations of lightning leaders during ASIM video  
190 frames. The CFAD (Yuter and Houze, 1995) is a two-dimensional histogram of radar  
191 reflectivity with height. The CFADs provide information on changes in the vertical  
192 distribution of radar reflectivity that help to identify the cloud depth and hydrometeors  
193 types above the altitude of the lightning leaders. For instance, narrow distributions with  
194 height imply homogenous precipitating sized particles, while bi-modal or broad  
195 distributions mean different types or size of hydrometeors.

196

### 197 **3. Results**

198

199 On November 22<sup>nd</sup> 2018, a lightning flash occurred at 08:57:21.4413 UT near  
200 Barrancabermeja (Colombia) at ~7.4° latitude and -73.85° longitude (Figure 1). The flash  
201 was in a cell of a large nighttime thunderstorm system within the coverage of the  
202 Colombia LMA in Barrancabermeja and ranging from 36 to 67 km from the radar. The  
203 initial part of the flash was outside the field of view of the MMIA sensors (white markers  
204 in the south-east view in Figure 1a and b) in a region with cloud top temperatures between

205 -73 °C and -75 °C, corresponding to heights of ~14.5 km according to ERA-INTERIM  
206 reanalysis (Dee et al., 2011). The part of the flash observed by ASIM (Figure 1c and black  
207 filled markers in Figure 1a and b) mostly developed in a less deep region with warmer  
208 cloud top temperatures of -66 °C to -68 °C (~13.5 km). For later analysis, the five regions  
209 (boxes) depicted in Figure 1-b and 1-c will be used to relate features of optical  
210 observations with lightning processes and cloud properties.

211

### 212 **3.1 The lightning flash**

213

214 The flash originated at 7.223°/-73.91° in the coldest cloud top (marker a in Figure 2).  
215 LMA sources in Figure 2 show that the flash initiation was at a height of 5 km with a  
216 negative leader propagating upwards at  $\sim 10^5$  m s<sup>-1</sup> up to 11 km. After ~50 ms (b), new  
217 negative leaders appeared at the same location as the previous one and expanded  
218 simultaneously to southward and northward directions for 450 ms (b-c). During this  
219 period, sources associated with positive leader breakdown were identified at a lower level,  
220 ~5 km altitude. The negative and positive leaders during the first 500 ms period of the  
221 flash (a-c) revealed the existence of positive polarity electric charge between 6 to 11 km  
222 altitude and negative electric charge below 5 km.

223

224 At 441.85 s new IC breakdown occurred at the north-end of the flash (c') at the time when  
225 a negative CG (-CG) stroke of -24 kA was detected by LINET and WWLLN. From the  
226 location of the -CG stroke, slow negative leaders ( $< 10^5$  m s<sup>-1</sup>) expanded radially 5 km for  
227 150 ms (c'-d and LMA sources in Box 1, Figure 1). After this time (d), a fast negative  
228 leader ( $\sim 10^5$  m s<sup>-1</sup>) was initiated from this area and propagated towards the east into a  
229 stratiform region for about 175 ms (d-f) and progressively descending from 9 km to 7 km  
230 altitude branching 40 ms (e) before ending (sources in Box 2, Figure 1). After the end of  
231 this leader (f), a positive +CG stroke with 11 kA occurred close to the location (f') of the  
232 earlier -CG stroke. As can be deduced from the presence and characteristics of the ELF  
233 transient waveform, the initiation of fast intracloud negative leaders (van der Velde and  
234 Montanyà, 2013; and van der Velde et al., 2014) and using a similar optical discrimination  
235 criterion as Bitzer (2016), we assume that this +CG produced continuing current. During  
236 this continuing current phase, a fast horizontal negative leader ( $0.4 \cdot 10^6$  m s<sup>-1</sup>) at < 7 km  
237 extended the propagation of the flash further east (g-h). This leader presented two

238 branches extending simultaneously towards the south-east (f-g and Box3, Figure 1) and  
239 to the north (f-h and Box 4, Figure 1). From the leader at the north, a branch propagated  
240 at  $0.5 \cdot 10^6 \text{ m s}^{-1}$  towards the north-east (h-j and Box 5, Figure 1). The flash ended with the  
241 end of this leader propagation followed by a short-isolated breakdown (k) at the northeast  
242 of the two CG locations.

243

244 In summary, this two-stroke bipolar CG flash started in a convective core of the storm  
245 with leaders propagating for 500 ms. A -CG stroke occurred at the north end of the  
246 previous leader activity followed by negative leader propagation into the stratiform region  
247 of the cloud for 300 ms. A +CG stroke followed at the location of the previous -CG stroke.  
248 This +CG stroke produced continuing current likely supplied by the propagation of a fast  
249 negative leader.

250

### 251 ***3.3 MMIA photometer, GLM and ISS-LIS radiances***

252

253 Altitudes of the located LMA sources versus time during MMIA detections are plotted in  
254 Figure 3a. Radiances measured by MMIA in the three spectral bands (337.0 nm, 777.4  
255 nm and 180-230 nm) are depicted in Figures 3-b, c and d. Radiances of ISS-LIS (red line)  
256 and GLM (black line) have been computed by integrating radiances from all the events  
257 detected every 2 ms frame (Figure 3-c). Since both ISS-LIS and GLM observe the 777.4  
258 nm spectral band, there is very high consistency with the same MMIA photometer spectral  
259 band (red line in Figure 3-b). Note that ISS-LIS (red line) radiance stops before GLM  
260 (black line) because the flash was no longer in the field of view of the sensor.

261

262 Inspecting the photometer radiances (Figure 3-b), after 442.05 s, the blue and red channels  
263 showed a progressive increase of radiance superimposed with small surges. At 442.15 s  
264 the red signal abruptly increased producing several peaks just before the +CG. This  
265 increase was also present in the GLM and ISS-LIS radiances. Just after the time of the  
266 +CG stroke, the peak was more pronounced in the red than in the blue band. The red pulse  
267 presented faster rise and decay times (2.2/12.9 ms) compared to the blue (5.4/71.1 ms).  
268 Starting right after the +CG stroke, the ELF magnetic field signal measured in Cape Verde  
269 (Figure 3-e) suggests the presence of continuing current. This continuing current is  
270 noticeable in the ELF signal for about 30 ms that corresponds to a decay to about 25 %  
271 of the peak value in the MMIA red and GLM radiances. The presence of continuing

272 current during this period is also supported by the identified LMA sources of a fast (0.4  
273  $10^6 \text{ m s}^{-1}$ ) negative leader. Note that the transients in the magnetic field occurring after  
274 442.25 s (Figure 3-e) might belong to a different flash, according to the detection of a  
275 distant flash at that time by GLM. The small signal in the MMIA 180-230 nm photometer  
276 (Figure 3-d), seems to present a small increase at the time of the +CG, and behaves more  
277 similarly to the blue band although its amplitude is more than three orders of magnitude  
278 smaller.

279

### 280 *3.4 MMIA imaging data and weather radar*

281

282 In the last four video frames recorded by MMIA, the flash was entirely in the field of  
283 view, so the previous frames have been omitted in this study. The periods of each video  
284 frame are indicated with vertical lines in Figure 3b and displayed in Figure 4. The four  
285 camera images of ASIM are shown in Figure 4 with the blue channel (337 nm) images in  
286 the left column and the red channel (777.4 nm) images in the right column. The location  
287 of the investigated boxes on the MMIA images can be easily identified in Figure 1c.

288 In the video frame 1 (Figure 4-a) the luminosity of the flash comes from the location of  
289 the -CG stroke that occurred 125 ms before the frame start and where the LMA detected  
290 some negative leader breakdown activity (Box 1 in Figure 1b and c). During frame 1, the  
291 LMA detected a new leader propagating out of what will become the main luminosity  
292 core towards the east (Box 2). This new leader is seen in both cameras, but remained  
293 undetected by GLM and ISS-LIS. The radar cross-sections along the LMA sources during  
294 this frame indicate that the sources occurred above the altitude of the 20 dBZ reflectivity  
295 echo tops. During frame 2, the leader entered into a more stratiform region (Box 2) with  
296 reflectivity <15 dBZ echo tops above the leader height (8 km) and coldest cloud top  
297 temperature of -67 °C (13.5 km). The leader is clearly seen in both MMIA cameras  
298 (Figure 4-b) and GLM reports events within the high radiance region in the red MMIA  
299 image. At the beginning of frame 3 (Figure 4-c), a +CG stroke located in Box 1 triggered  
300 a fast negative leader ( $0.4 \cdot 10^6 \text{ m s}^{-1}$ ) that propagated and branched during the frame  
301 exposure. The branch towards the southeast (Box 3) produced more LMA sources than  
302 the branch that propagated to the north (Box 4) but only the latter is well identified in the  
303 red image. Figure 4-d depicts frame 4 where the leader propagating to the north-east (Box  
304 5) can be more easily distinguished in the red image than in the blue. It is also remarkable  
305 that the section of leader end appears brighter than its channel behind. The north-east

306 branch (Box 5) is responsible for the radiance peak after 442.25 s in the MMIA red  
307 channel photometer (Figure 3-b) and GLM (Figure 3-c), this will be discussed in the  
308 section 4.2.

309

310 To relate cloud properties with the optical observations, two-dimensional histograms of  
311 radar reflectivity with height, contoured-frequency-by-altitude diagrams (CFAD) are  
312 computed along the leader propagation paths in Figure 1b and shown in Figure 5. Box 1  
313 corresponds to the area where the CG strokes were located; and Box 2 includes the area  
314 within  $\pm 1$  radial gate (representing 750 m width) along the central leader channel mapped  
315 by the LMA during frames 1, 2 before it branches. Box 3 and 4 are analogous to Box 2  
316 for southeast and north branches during frames 3 and 4, respectively; and the same in Box  
317 5 of the leader branch towards the northeast. In each CFAD, the altitude of the leader is  
318 indicated by the heavy horizontal dashed line whereas the 50<sup>th</sup> and 90<sup>th</sup> percentiles of the  
319 cumulative reflectivity  $Z$  are indicated by the solid and dashed lines, respectively.

320

321 The LMA sources within Box 1 are located at an altitude of  $\sim 9$  km (Figure 2). At this  
322 altitude, the CFAD (Figure 5-a) shows a thinner region with weak  $Z$  values with 90 % of  
323 the reflectivity below 18 dBZ. In this area, the maximum radiances of the flash in both  
324 spectral channels are found in frame 3 (Figure 4-c) when the +CG stroke occurred. The  
325 peak in the measured red photometer is higher than the one recorded by the blue  
326 photometer. In the same region defined by Box 1, the blue signal surpasses the red after  
327 the continuing current during frame 5 (figure 4-d). In Box 2, the CFAD shows a shallow  
328 cloud above the leader height at  $\sim 8$  km with 90 % of the reflectivity below  $\sim 17$  dBZ. This  
329 low reflectivity and the shallow cloud above the leader channel did not prevent the  
330 lightning leader at this location to be imaged in frames 1 and 2. Much higher reflectivity  
331  $< 23$  dBZ is found above the south-west lightning leader channel in Box 3 that propagates  
332 at 7.5 km altitude. Although Box 3 has low cloud tops according to the radar and satellite  
333 images, and the lightning leader channel is close to the top, the high reflectivity above the  
334 channel is an indication of high concentration and/or large size of cloud particles. The  
335 dense cloud in Box 3 could be responsible for the almost undetectable luminosity from  
336 the lightning channels there. In Box 4, the north leader channel propagates during frame  
337 3 at an altitude of 7 km with a reflectivity of the cloud above it of  $< 18$  dBZ. In this area  
338 luminosity of the leader is much higher in the red than in the blue image (Figure 3-c).  
339 Finally, the cloud in Box 5 has convective characteristics as indicated by its cloud tops in

340 Figure 1 and the reflectivity profile in Figure 5. The north-east leader in Box 5 during  
341 frame 4d is clear in the red image and well tracked by GLM, but highly attenuated and  
342 diffuse in the blue. The leader travels at 7 km and above this level we found reflectivity  
343 of  $<20$  dBZ.

344

## 345 4. Discussion

346

### 347 4.1 Radiances and radar reflectivity

348

349 The average blue (337.0 nm) and red (777.4 nm) radiances observed by the ASIM  
350 cameras of the five selected boxes are shown in Figure 6.

351

352 At the location of the CG strokes (Box 1), lightning leader sources are identified at an  
353 altitude of  $\sim 9$  km with a shallow cloud of low reflectivity ( $< 18$  dBZ) above it. This may  
354 have produced little attenuation compared to other deeper areas. The ratio of the received  
355 red to blue starts with values from  $\sim 1.85$  during the frames 1 and 2 before the +CG stroke.  
356 At the time of the +CG stroke (frame 3), radiances peak and the ratio increases to 2.2.  
357 The ratio remains higher than 1 for the 30 ms corresponding to the continuing current  
358 phase until both radiances equalize. Later, in frame 4, the ratio of the average radiance  
359 decreases to 0.9 (0.6 for the peak radiances not shown in Figure 6), meaning that the  
360 received blue radiance is more intense than the red. From Figures 3 and 4, the consistency  
361 of the red radiance with the continuing current suggests that the observed red channel  
362 (777.4 nm) oxygen atomic line is more related with the evolution of lightning currents  
363 than the blue band. The relation of red radiance pulses with impulsive lightning current  
364 events identified by the LMA was previously observed by *Thomas et al.* (2000). In the  
365 laboratory, *Windmar et al.* (1991) found a proportional relation of the peak amplitude of  
366 the red radiance with the kiloampere current of a long spark. The relation of the 777.4 nm  
367 emission is related with hot lightning channels ( $>4000$  K) or sparks that provide thermal  
368 excitation of the  $^5P$  electronic state of atomic oxygen (see the interpretation in *Soler et*  
369 *al.*, 2020). In Box 1 the slow decay of the blue signal different to the red may indicate the  
370 prevalence of streamer/corona or other low temperature discharge activity, in particular,  
371 at the region of the location of the CG strokes. So, whereas the reduction of the red  
372 emission has been related to the decay of the continuing current, the prevalent blue  
373 optical emissions are assumed to come from the streamer/corona accompanying the high-

374 altitude negative leader channel at this region. This channel is the root of the channels  
375 progressing along the other boxes. Blue emissions are common in streamer and corona  
376 discharges and are related to the  $N_2$  2<sup>nd</sup> positive system and the  $N_2^+$  1<sup>st</sup> negative system  
377 (e.g. *Soler et al.* 2020 and references therein). In the laboratory, works such as *Machala*  
378 *et al.* (2011) and *Janda et al.* (2016) showed the emission of the  $N_2$  2<sup>nd</sup> positive system at  
379 the 337.0 nm being associated with the streamer phase of a spark discharge. So, the  
380 identified prevalence of the blue signal might be related to the evolution of the electric  
381 fields related with the leaders and the cloud.

382

383 The radiance in Box 2 includes the leader channel emerging from the location of the CG  
384 strokes at frame 1. This negative leader propagated at  $10^5$  m s<sup>-1</sup> and ended at the time of  
385 the +CG (frame 3). From this central leader channel two branches occurred after the +CG  
386 corresponding to the LMA sources in Box 3 and 4. At the time of frame 3, the central  
387 leader channel presented higher red radiance than its south-east, north and north-east  
388 branches in Boxes 3, 4 and 5, respectively. As seen in Figure 5 and Figure 6, at the regions  
389 of the south-east (Box 3), north (Box 4) and north-east (Box 5), the cloud above the leader  
390 was thicker in terms of reflectivity than in Box 2. This thicker cloud mostly affected the  
391 blue band. This is reflected in the ratios of the average radiance in Figure 5-b, c, d and e  
392 at the time of frame 3 corresponding to 2.9 (18 dBZ), 3.8 (23 dBZ), 4 (18 dBZ) and 5.4  
393 (20 dBZ), respectively. The reflectivity in parentheses correspond to the maximum above  
394 the leader. During this frame, the charge that feeds the continuing currents to ground is  
395 assumed to be provided by the south and north leader branches based on the fast  
396 propagation ( $0.4 \cdot 10^6$  m s<sup>-1</sup>) of the leaders and their higher radiances compared to the  
397 extension of the north-east leader.

398

399 One of the salient features of the observation is the imaged north-east leader branch (Box  
400 5) by the red camera at frame 4 (Figure 4-d). This leader end produced an increase in the  
401 777.4 nm radiance after 442.25 s (Figure 3b) which is not observed in the blue channel  
402 image. The level of the blue radiance in Box 5 during frame 4 corresponds almost to the  
403 background level and it is lower than the corresponding radiance at the same frame but  
404 in the leader channel behind in Box 2. For comparison, the red radiance during frame 4  
405 is ~1.2 times greater in Box 5, at the leader end, compared to its trailing channel in Box  
406 4 and Box 2 although Box 5 had the deepest cloud above the leader. This negative  
407 correlation between the radiance and radar reflectivity suggests that the detected surge in

408 the radiation might be related with the occurrence of some intra-cloud process involving  
409 high currents (e.g. recoil leader event) at the leader end in Box 5.

410

411 In addition, taking into account that the used weather radar is more sensitive to the back-  
412 scatter of ice and water particles and these precipitating ice particles are related to icy  
413 cloud particles (*Baker et al., 1999*), it is plausible to state that the higher the ice content  
414 above 8 km the higher will be the concentration of cloud ice particles. Moreover, the  
415 broader the CFAD distributions above the freezing level, the more ice cloud particles are  
416 produced reflecting higher updrafts that consequently produce more super-saturation.  
417 Therefore, the optical emissions would be more attenuated depending on the  
418 concentration and the size of ice particles above the leader (*Brunner and Bitzer, 2020*,  
419 *Rutledge et al., 2020*) as well as on the water vapor (*Thomason and Krider 1982*) that  
420 fed those particles. At Box 3, the higher and large sized ice cloud particles concentration  
421 attenuated both the red and blue channels, while at Boxes 4 and 5, the presence of more  
422 water vapor and smaller ice cloud particles might have contributed to enough attenuation  
423 of both spectral bands. The north and north-east leaders (Box 4 and 5) may have produced  
424 sufficiently high currents to generate detectable levels of red emissions. In the Section 4.3  
425 a quantitative analysis of the cloud optical depths at the considered regions is presented.

426

427 In summary, the red radiance is close related to the occurrence of the currents on the  
428 leader channels according to the identified CG strokes, continuing currents and the recoil  
429 leader event consistently with previous works (e.g. *Thomas et al., 2000*). The longer time  
430 decay of the blue emissions relative to the red and their lower correlation with the  
431 evolution of the currents can be indicative that these blue emissions are related to the  
432 streamer zones of the leader channels according to the nature of the blue emission ( $N_2$   
433  $2^{nd}$  positive system). So, blue emissions would be related to the evolution of the electric  
434 fields of the leader and the cloud. Nevertheless, the detected blue radiation allows imaging  
435 of the leader channels in the regions with less cloud above the lightning flash.

436

#### 437 ***4.2 Surges of radiance associated with leader branching***

438

439 The small surges in red and blue emissions at 442.127 s in Figure 3b during frame 2  
440 (marker e) are related to a new branch of the developing leader. This branch continues for  
441 40 ms until the time of the +CG stroke. This leader branch can be associated with the

442 downward positive leader approaching the ground, including the last 12 ms where both  
443 the blue and red radiances increased, oscillating in the red. This oscillation is consistent  
444 with the impulsive optical emissions by recoil leader events (K-changes) analysed by  
445 (*Montanyà et al.* 2012) using high speed video during the development of positive leader  
446 to ground. Impulsive red optical emissions related to recoil leader events were previously  
447 reported by *Thomas et al.* (2000). About 50 ms after the +CG stroke (frame 3), at 442.226  
448 s, a new radiance surge in the red channel is associated with new negative leader branches  
449 (from g and h in Figure 2) propagating for 20 ms with speeds  $0.4 \cdot 10^6 \text{ ms}^{-1}$  (Box 3, 4).  
450 Finally, the red surge at 442.256 s in frame 4, Box 5, also occurred in association with a  
451 leader branching and further propagation (i-j in Figure 2). In the blue photometer, these  
452 surges are unnoticed at the indicated times although there are some smoothed and delayed  
453 pulses that might be related. This is the case of the peak in the blue at 442.226 s occurring  
454 7 ms after the peak in the red (Figure 3-b). If both peaks are related, then the significant  
455 delay might be due to the blue radiance originating from the region of the CG stroke (Box  
456 1) whereas the red originates from the location of the leader branching (Box 3, 4). Possible  
457 delays due to higher scattering in the blue than in the red are possible (e.g. *Luque et al.*,  
458 2020).

459

### 460 **4.3 Optical depth**

461

462 *Light et al.* (2001) and *Beirle et al.* (2014), among others, stated that clouds mostly affect  
463 the propagation of light causing spatial smearing via multiple scattering. Light absorption  
464 by ice and water at the 337.0 nm and 777.4 nm is small (e.g. *Warren*, 1984; *Thomason*  
465 *and Krider*, 1982; *Light et al.*, 2001; *Warren and Brandt*, 2008) but the absorption and  
466 scattering differences can be significant between the two wavelengths (*Luque et al.*,  
467 2020). Some previous works (e.g. *Thomason and Krider*, 1982; *Koshak et al.*, 1994;  
468 *Thomas et al.* 2000; *Light et al.* 2001, *Brunner and Bitzer*, 2020) found that the optical  
469 depth between the light source and the cloud edges including the horizontal extension of  
470 the cloud (*Koshak et al.*, 1994) highly affects the detectability of lightning. These works  
471 also indicate the need to know the location and the progression of the source within the  
472 cloud. *Rutledge et al.* (2020) found that optical emissions are not completely correlated  
473 with the ice water path above individual lightning flashes derived from radar data because  
474 the precipitating particles detected by radar are not necessarily the main reason for the

475 light attenuation. Small undetectable cloud particles may have higher concentrations and  
476 so can produce collectively higher light attenuation than precipitation-size particles.

477 We now attempt to evaluate the effects of the cloud on the light propagation at the  
478 investigated regions of the flash. Due to the radar limitations, we adopt the cloud particle  
479 distribution from vertical radar reflectivity and temperature profiles using the  
480 parametrization by *Heymsfield et al.* (2002 and 2013). The calculated particle  
481 distributions at each level are limited from a minimum diameter of 20  $\mu\text{m}$  up to a  
482 parametrized maximum diameter. Optical depth of the cloud sections above the lightning  
483 leader channels at each box are calculated by following *Thomason and Krider* (1982).  
484 Optical depths are limited up to an altitude of 10 km because, as pointed out by *Rutledge*  
485 *et al.* (2020), we found unrealistically high particle densities for the low temperatures at  
486 higher levels. Details on the calculations of particle distribution and optical depth are  
487 provided in the Appendix section of this paper. Results of the estimated optical depths are  
488 presented in Table 1. The values are relative to the optical depth in Box 1. We present  
489 relative optical depths because of the high sensitivity of the cloud particle distribution on  
490 the temperature (*Heymsfield et al.* 2002 and 2013). Despite this dependence, the relative  
491 optical depths between boxes remain almost independent to temperature offsets. The  
492 calculated relative optical depths are consistent with some of the characteristics of the  
493 observed radiance from each box. The lower optical depth of Box 2 relative to Box 1 is  
494 in accordance with the more stratiform nature of the cloud in this region where the red  
495 and blue radiances were less effected by cloud. The reduction of 50 % of the optical depth  
496 in Box 2 results from the decrease of 3 dBZ and a shallower cloud above the leader  
497 compared to Box 1. In contrast, Box 3 presents the highest relative optical depth  $\sim 2$   
498 coinciding with the region with the almost undetected blue and red radiances. Compared  
499 to Box 1, despite the fact that the median reflectivity above the leader is 1 dBZ higher,  
500 the maximum reflectivity (90<sup>th</sup> percentile) is 6 dBZ greater and with lower lightning  
501 leader channel height. In between, the 0.9 relative optical depth of Box 5 allowed the  
502 detection of the red emissions but strongly attenuated the blue. Figure 1a shows a higher  
503 cloud top in Box 5 if compared to Box 4 and similar to the cloud tops in Box 1. The  
504 median reflectivity in Box 5 at the leader altitude is 2 dBZ lower than in Box 1 whereas  
505 the reflectivity corresponding to the 90<sup>th</sup> percentile is 3 dBZ higher.

506

507 In summary, to overcome the limitation of radar on the detection of cloud particles the  
508 parametrized ice particle size distributions employed have provided consistent relative

509 optical depth with the optical observations. Consistently with *Brunner and Bitzer (2020)*,  
510 the results highlight the importance on the combination of the light emission by different  
511 lightning processes and the optical depth features due to cloud ice particles surrounding  
512 the lightning channels at high cloud altitudes (>7 km). The location at Box 1 where the  
513 return stroke currents produced high channel luminosity and with low cloud optical depth  
514 due to lightning channels at high altitudes, would be evidence of the CG features pointed  
515 out by *Zhang and Cummins (2020)* to produce high detection efficiency of CG flashes by  
516 GLM. In the area of the lowest relative optical depth (Box 2) corresponding to a stratiform  
517 region, the propagation of negative lightning leaders has been optically resolved by  
518 MMIA and GLM. The detection of this leader by GLM might have been made possible  
519 by the occurrence of a branching of the leader that produced a surge in the radiance  
520 (marker e in Figure 3-b) if compared to the undetected leader by GLM in frame 1 (Figure  
521 4-a). The increase of a factor of 2 on the relative optical depth in Box 3 attenuated the  
522 optical emissions of a fast negative leader producing abundant LMA sources. The  
523 undetected leader did not present any feature such as branching or recoil leader that might  
524 had involved a surge in channel luminosity. Box 5 with lower optical depth than Box 1  
525 and a surge in radiance, allowed GLM to image the propagation of the leader (Figure 4-  
526 d) all along the channel from the tip to the location of the former CG. Our results  
527 complement the recent study by *Rutledge et al. (2020)*. Instead of using the ice water path  
528 derived from radar we have estimated the cloud particle size distribution from  
529 parametrization data and we have found consistency with the observations. In addition,  
530 we have investigated the features in different parts of the flash considering their cloud  
531 and lightning features. Nevertheless, for a precise evaluation of the light escaping from  
532 the cloud, cloud edges and the horizontal cloud extension (*Koshak et al., 1994*) should  
533 not be omitted.

534

## 535 **5. Conclusions**

536

537 We have presented concurrent measurements of a lightning flash from space by ASIM,  
538 GLM, ISS-LIS and from the ground by the Colombia-LMA, WWLLN, a local weather  
539 radar, and an ELF electromagnetic wave receiver. This observation has provided the  
540 means for interpretation of the optical observations with respect to lightning leader  
541 processes. This flash included negative and positive strokes as well the occurrence of  
542 continuing currents. In addition, weather radar data allowed estimation of the attenuation

543 of optical radiance by the clouds above the lightning leaders at different locations along  
544 the path of the lightning channel propagation.

545

546 The following summarizes our findings:

547

548 • Surges in the photometer radiance, especially in red (777.4 nm), besides return  
549 stroke and recoil leader processes have been found to be associated with lightning  
550 leader branching involving new leader development. These surges associated to  
551 leader branching are not always noticed in the blue (337.0 nm) signals, so these  
552 processes appear not to involve significant emissions in this wavelength.

553 • The radiance at red correlates with the continuing current identified from the  
554 magnetic ELF signals, the fast leader development detected by the LMA and the  
555 continuous radiance.

556 • The oscillations in the red signal photometer just before the +CG stroke are  
557 probably recoil leader events during the downward propagation of the leader to  
558 ground prior to the return stroke.

559 • Based on the above, the detected red signals are likely from the highly conducting  
560 hot leader channels and associated with high luminosity of the channel involving  
561 impulsive and continuing current processes.

562 • The camera images showed long persistence of blue radiation at the location of  
563 the +CG stroke after the decay of the continuing current and even surpassing the  
564 detected red radiance.

565 • The blue emission has been shown to not be closely related to lightning current  
566 processes. The nature of the  $N_2$  2<sup>nd</sup> positive system optical emission suggests the  
567 origin from non-thermal discharges (streamers) on the leader channels and  
568 probably in the thundercloud.

569 • The detected blue radiation allowed imaging of the leader channels especially in  
570 the stratiform areas with low cloud tops.

571 • Cloud depth or cloud thickness above the lightning channels appears to attenuate  
572 more to the blue emission more than the red.

573 • Relative optical depths at different parts of the cloud where lightning leaders  
574 propagated have been estimated from radar and temperature data using  
575 parametrized models of particle size distribution.

576 • Besides the position of the lightning leaders and the properties of the cloud above  
577 and around them, detection of optical emissions of lightning depends on the  
578 different lightning processes, which can be inferred from their temporal and  
579 spectral properties.

580

## 581 **Acknowledgments**

582

583 This work was supported by research grants from the Spanish Ministry of Economy and  
584 the European Regional Development Fund (FEDER): ESP2013-48032-C5-3-R,  
585 ESP2015-69909-C5-5-R, ESP2017-86263-C4-2-R and PID2019-109269RB-C42. ASIM  
586 is a mission of ESA's SciSpace Programme for scientific utilization of the ISS and non-  
587 ISS space exploration platforms and space environment analogues. It is funded by ESA  
588 and national contributions through contracts with TERMA and Technical University of  
589 Denmark (DTU) in Denmark, University of Bergen (UB) in Norway and University of  
590 Valencia (UV) in Spain. The ASIM Science Data Centre (ASDC) at DTU is supported  
591 by PRODEX contract PEA 40001 1 5884. The authors are grateful to Keraunos for  
592 providing LINET lightning data and the World Wide Lightning Location Network  
593 (<http://wwlln.net/>) for providing WWLLN lightning location data. Also, we would like to  
594 thank the Colombian Instituto de Hidrología, Meteorología y Estudios Ambientales  
595 (IDEAM) for providing the weather radar information used in this study.

596

597

## 598 **Data availability**

599 Data associated with this work will be made available in the Zenodo scientific repository.  
600 Data access to ASIM is available by registering at <https://asdc.space.dtu.dk/>. GLM data  
601 are available from NOAA (GOES-R Series Program, 2019,  
602 <https://data.nodc.noaa.gov/cgi-bin/iso?id=gov.noaa.ncdc:C01527#>) and ISS-LIS from  
603 NASA Global Hydrology Resource Center (*Blakeslee et al. 2019*,  
604 <https://ghrc.nsstc.nasa.gov/pub/lis/iss/data/science/nqc/hdf/>). The ABI imagery can be  
605 accessed from the NOAA's Comprehensive Large Array Storage Service (CLASS) or the  
606 Google ([gcp-public-data-goes-16](https://gcp-public-data-goes-16)) or Amazon cloud.

607

608

609

610 **References**

611

612 Aranguren, D., López, J., Inampué, J., Torres, H., and Betz, H. D. (2017). Cloud-to-ground lightning  
613 activity in Colombia and the influence of topography *Journal of Atmospheric and Solar-Terrestrial Physics*,  
614 doi: 10.1016/j.jastp.2016.08.010.

615

616 Baker, M. B., Blyth, A. M., Christian, H. J., Latham, J., Miller, K. L., and Gadian, A. M. (1999).  
617 Relationships between lightning activity and various thundercloud parameters: satellite and modelling  
618 studies. *Atmospheric Research*, 51, 221-236.

619

620 Beirle, S., Koshak, W., Blakeslee, R., and Wagner, T., (2014). Global patterns of lightning properties  
621 derived by OTD and LIS. *Nat. Hazards Earth Syst. Sci.*, 14, 2715–2726.

622

623 Bitzer, P. M. (2017). Global distribution and properties of continuing current in lightning. *J. Geophys. Res.*  
624 *Atmos.*, 122, 1033–1041, doi:10.1002/2016JD025532.

625

626 Betz H. D., Schmidt, K., and Oettinger W. (2009). LINET – An International VLF/LF Lightning Detection  
627 Network in Europe. *Lightning: Principles, Instruments and Applications*. Springer, doi: 10.1007/978-1-  
628 4020-9079-0\_5.

629

630 Blakeslee, R. J. (2019). Non-Quality Controlled Lightning Imaging Sensor (LIS) on International Space  
631 Station (ISS) Science Data. NASA EOSDIS Global Hydrology Resource Center Distributed Active Archive  
632 Center, Huntsville, Alabama, U.S.A. doi:10.5067/LIS/ISSLIS/DATA107. [Accessed: 11 March 2020]

633

634 Blakeslee, R. J., Lang, T. J., Koshak, W. J., Buechler, D., Gatlin, P., Mach, D. M., Stano, G. T., Virts, K.  
635 S., Walker, T. D., Cecil, D. J., Ellett, W., Goodman, S. J., Harrison, S., Hawkins, D. L., Heumesser, M.,  
636 Lin, H., Maskey, M., Schultz, C. J., Stewart, M., Bateman, M., Chanrion, O., and Christian, H. (2020).  
637 Three years of the Lightning Imaging Sensor onboard the International Space Station: Expanded Global  
638 Coverage and Enhanced Applications. *Earth and Space Science*, <https://doi.org/10.1002/essoar.10502896.1>.

639

640 Boccippio, D. J., Williams, E. R., Heckman, S. J., Lyons, W. A., Baker, I. T., and Boldi, R. (1995). Sprites,  
641 ELF transients, and positive ground strokes. *Science*, 269, 1088.

642

643 Burke, C. P., and Jones, D. L. (1996). On the polarity and continuing currents in unusually large lightning  
644 flashes deduced from ELF events. *J. Atmos. Terr. Phys.*, 58, 531.

645

646 Brunner K. N., and Bitzer, P. M. (2020). A first look at cloud inhomogeneity and its effect on lightning  
647 optical emission. *Geophysical Research Letters*, 47, e2020GL087094. [https://doi.org/](https://doi.org/10.1029/2020GL087094)  
648 10.1029/2020GL087094.

649

650 Cáceres-Leon, R. (2017). Meteorología Aplicada a la Seguridad de las Operaciones Aéreas, Colección  
651 Ciencia y Poder Aéreo, ISBN: 978-958-59961-1-3.  
652 [Available online: <https://libros.publicacionesfac.com/index.php/libros/catalog/book/22>].  
653  
654 Chanrion, O., Neubert, T., Lundgaard Rasmussen, I., et al. (2019). The Modular Multispectral Imaging  
655 Array (MMIA) of the ASIM Payload on the International Space Station. *Space Sci. Rev.*, 215, 28.  
656 <https://doi.org/10.1007/s11214-019-0593-y>.  
657  
658 Christian, H. J., and Goodman, S. J. (1987). Optical observations of lightning from a high altitude airplane.  
659 *J. Atmos. Ocean. Tech.*, 4, 701-711.  
660  
661 Christian, H. J., R. J. Blakeslee, and S. J. Goodman (1989), The detection of lightning from geostationary  
662 orbit, *J. Geophys. Res.*, 94, 13329–13337.  
663  
664 Dee, D. P., Uppala, S. M., Simmons, A. J., Berrisford, P., Poli, P., Kobayashi, S., ... and Bechtold, P. (2011).  
665 The ERA-Interim reanalysis: Configuration and performance of the data assimilation system. *Quarterly*  
666 *Journal of the Royal Meteorological Society*, 137(656), 553-597.  
667  
668 Erdmann, F., Defer, E., Caumont, O., Blakeslee, R. J., Pédeboy, S., and Coquillat, S. (2020). Concurrent  
669 Satellite and ground-based Lightning Observations from the Optical Lightning Imaging Sensor (ISS-LIS),  
670 the LF network Meteorage and the SAETTA LMA in the northwestern Mediterranean region. *Atmos.*  
671 *Meas. Tech.*, 13, 853–875.  
672  
673 GOES-R Algorithm Working Group and GOES-R Series Program, (2018): NOAA GOES-R Series  
674 Geostationary Lightning Mapper (GLM) Level 2 Lightning Detection: Events, Groups, and Flashes. NOAA  
675 National Centers for Environmental Information. doi:10.7289/V5KH0KK6.  
676  
677 Goodman, S. J., H. J. Christian, and Rust, W.D. (1988). Optical pulse characteristics of intracloud and  
678 cloud-to ground lightning observed from above clouds, *J. Appl. Met.*, 27, 1369-1381.  
679  
680 Goodman, S. J., Blakeslee, R. J., Koshak, W. J., Mach, D., Bailey, J., Buechler, D., Carey, L., Schultz, C.,  
681 Bateman, M., McCaul, E., and Stano, G. (2013). The GOES-R Geostationary Lightning Mapper (GLM).  
682 *Atmospheric Research*, 125-126, 34– 49.  
683  
684 Heymsfield, A. J., Bansemmer, A. , Field, P. R., Durden, S. L., Stith, J., Dye, J. E., Hall, W., and Grainger  
685 T. (2002). Observations and parameterizations of particle size distributions in deep tropical cirrus and  
686 stratiform precipitating clouds: Results from in situ observations in TRMM field campaigns. *J. Atmos. Sci.*,  
687 59, 3457–3491.  
688

689 Heymsfield, A. J., Schmitt, C., and Bansemer, A. (2013). Ice Cloud Particle Size Distributions and  
690 Pressure-Dependent Terminal Velocities from In Situ Observations at Temperatures from 0° to -86°C. *J.*  
691 *Atmos. Sci.*, 70, 4123–4154.

692

693 Huang, E., Williams, E., Boldi, R., Heckman, S., Lyons, W., Taylor, M., Nelson, T., and Wong, C. (1999).  
694 Criteria for sprites and elves based on Schumann resonance observations. *J. Geophys. Res.*, 104(D14),  
695 16943-16964.

696

697 Koshak, W. J., Solakiewicz, R. J., Phanord, D. D., and Blakeslee, R. J. (1994). Diffusion model for lightning  
698 radiative transfer. *J. Geophys. Res.*, 99, 14361-14371.

699

700 Light, T. E., Suczynsky, D. M., Kirkland, M. W., and Jacobson, A. R. (2001). Simulations of lightning  
701 optical waveforms as seen through clouds by satellites. *J. Geophys. Res.*, 106 (D15), 17103–17114.  
702 <https://doi.org/10.1029/2001JD900051>

703

704 López J. A., Montanyà, J., van der Velde, O. A., Pineda, N., Salvador, A., Romero, D., Aranguren, D. and  
705 Tabora, J. (2019). Charge structure of two tropical thunderstorms in Colombia. *J. Geophys. Res.:*  
706 *Atmospheres*, [doi.org/10.1029/2018JD029188](https://doi.org/10.1029/2018JD029188).

707

708 Liu, H., and V. Chandrasekar, 2000: Classification of Hydrometeors Based on Polarimetric Radar  
709 Measurements: Development of Fuzzy Logic and Neuro-Fuzzy Systems, and In Situ Verification. *J. Atmos.*  
710 *Oceanic Technol.*, 17, 140–164, [https://doi.org/10.1175/1520-0426\(2000\)017<0140:COHBOP>2.0.CO;2](https://doi.org/10.1175/1520-0426(2000)017<0140:COHBOP>2.0.CO;2).

711

712 Luque, A., Gordillo-Vázquez, F. J., Li, D., Malagón-Romero, A., Pérez-Invernón, F. J., Schmalzried, A.,  
713 Soler, S., Chanrion, O., Heumesser, M., Neubert, T., Reglero, V., and Østgaard N., (2020). Modeling  
714 lightning observations from space-based platforms (CloudScat.jl 1.0). *Geoscientific Model Development*,  
715 [doi.org/10.5194/gmd-2020-161](https://doi.org/10.5194/gmd-2020-161).

716

717 Montanyà, J., van der Velde, O. A., March, V., Romero, D., Solà, G., and Pineda, N. (2012). High-speed  
718 video of lightning and X-ray pulses during the 2009–2010 observation campaigns in northeastern Spain.  
719 *Atmos. Res.*, 117, doi: 10.1016/j.atmosres.2011.09.013.

720

721 Montanyà, J., van der Velde, O. A., Pineda, N., and López, J.A. (2019). ISS-LIS data analysis based on  
722 LMA networks in Europe. EUMETSAT Science Studies, [Available online:  
723 [https://www.eumetsat.int/website/home/Data/ScienceActivities/ScienceStudies/ISSLISDataAnalysisBase](https://www.eumetsat.int/website/home/Data/ScienceActivities/ScienceStudies/ISSLISDataAnalysisBasedonLMANetworksinEurope/index.html#OB)  
724 [donLMANetworksinEurope/index.html#OB](https://www.eumetsat.int/website/home/Data/ScienceActivities/ScienceStudies/ISSLISDataAnalysisBasedonLMANetworksinEurope/index.html#OB)].

725

726 Neubert, T., Østgaard, N., Reglero, V., Blanc, E., Chanrion, O., Oxborrow, C. A., Orr, A. , Tacconi, M.,  
727 Hartnack, O., and Bhandari, D. D. V. (2019). The ASIM mission on the International Space Station. *Space*  
728 *Sci. Rev.*, 215:26 <https://doi.org/10.1007/s11214-019-0592-z>.

729

730 Peterson, M. (2019). Using lightning flashes to image thunderclouds. *J. Geophys. Res.: Atmospheres*, 124.  
731 <https://doi.org/10.1029/2019JD031055>

732

733 Peterson, M. J. (2014). Variations of optical and radio lightning characteristics and the relationship between  
734 storm convective intensity and above-cloud electric fields. Dissertation, The University of Utah, 253 pp  
735 [Available online at: [https://search.proquest.com/openview/2d481bb6a222ae8958de1016fd602870/1?pq-](https://search.proquest.com/openview/2d481bb6a222ae8958de1016fd602870/1?pq-origsite=gscholar&cbl=18750&diss=y)  
736 [origsite = gscholar&cbl = 18750&diss = y](https://search.proquest.com/openview/2d481bb6a222ae8958de1016fd602870/1?pq-origsite=gscholar&cbl=18750&diss=y)].

737

738 Rison, W., Thomas, R., Krehbiel, P., Hamlin, T., and Harlin, J. (1999). A GPS-based three dimensional  
739 lightning mapping system: Initial observations in central New Mexico. *Geophysical Research Letters*, doi:  
740 10.1029/1999GL010856.

741

742 Rodger, C.J., Werner, S., Brundell, J. B., Lay, E. H., Thomson, N. R., et al. (2006). Detection efficiency  
743 of the VLF World-Wide Lightning Location Network (WWLLN): initial case study. *Annales Geophysicae*,  
744 European Geosciences Union, 24 (12), 3197-3214.

745

746 Rutledge, S.A., Hilburn, K. A., Clayton, A., Fuchs B., and Miller, S. D. (2020). Evaluating Geostationary  
747 Lightning Mapper flash, *Journal of Geophysical Research: Atmospheres*, 125, Special Section: A New Era  
748 of Lightning Observations from Space. doi: 10.1029/2020JD032827.

749

750 Rudlosky, S., Goodman, S. J., and Virts, K. S. (2019a). Lightning detection: Geostationary Lightning  
751 Mapper, The GOES-R series: A new generation of geostationary environmental satellites pp. ISBN– 13:  
752 978–0128143278, ISBN–10: 0128143274): Academic Press; Amsterdam, The Netherlands.  
753 <http://www.worldcat.org/oclc/1127541502>.

754

755 Rudlosky, S. D., Goodman, S. J., Virts, K. S., & Bruning, E. C. (2019b). Initial Geostationary Lightning  
756 Mapper observations. *Geophysical Research Letters*, 46, 1097– 1104.  
757 <https://doi.org/10.1029/2018GL081052>

758

759 Soler, S., Pérez-Invernón, F. J., Gordillo-Vázquez, F. J., Luque, A., Li, D., Malagón-Romero, A., et al.  
760 (2020). Blue optical observations of narrow bipolar events by ASIM suggest corona streamer activity in  
761 thunderstorms. *Journal of Geophysical Research: Atmospheres*, 125, e2020JD032708.  
762 <https://doi.org/10.1029/2020JD032708>

763

764 Stuhlmann, R., Rodriguez, A., Tjemkes, S., Grandell, J., Arriaga, A., Bézy, J.-L., Aminou, D., and Bensi,  
765 P. (2005). Plans for EUMETSAT's third generation Meteosat Geostationary Satellite Programme, *Advances*  
766 *in Space Research*, 36(5), 975– 981.

767

768 Thomas, R. J., Krehbiel, P. R., Rison, W., Hamlin, T., Boccippio, D. J., Goodman, S. J., and Christian, H.  
769 J. (2000), Comparison of ground based 3-dimensional lightning mapping observations with satellite-based  
770 LIS observations in Oklahoma, *Geophysical Research Letters*, 27 (12), 1703–1706.  
771 <https://doi.org/10.1029/1999GL010845>.  
772

773 Thomas, R. J., Krehbiel, P. R., Rison, W., Hunyady, S., Winn, W., Hamlin, T., and Harlin, J. (2004).  
774 Accuracy of the lightning mapping array. *Journal of Geophysical Research: Atmospheres*, doi:  
775 10.1029/2004JD004549.  
776

777 Thomason, L. W., and E. P. Krider (1982). The effects of clouds on the light produced by lightning. *J.*  
778 *Atmos. Sci.*, 39, 2051-2065.  
779

780 van der Velde, O. A., and Montanya, J. (2013). Asymmetries in bidirectional leader development of  
781 lightning flashes. *J. Geophys. Res. Atmos.*, 118, 13,504–13,519, doi:10.1002/2013JD020257.  
782

783 van der Velde, O. A., Montanya J., Soula S., Pineda N., and Mlynarczyk J. (2014). Bidirectional leader  
784 development in sprite-producing positive cloud-to-ground flashes: Origins and  
785 characteristics of positive and negative leaders. *J. Geophys. Res. Atmos.*, 119, 12,755–12,779,  
786 doi:10.1002/2013JD021291.  
787

788 van der Velde, O., Montanya, J., Neubert, T., Chanrion, O., Lopez, J. A., Fabro, F., Østgaard, N., Goodman,  
789 S., and Reglero, V. (2020), Comparison of high-speed optical observations of a lightning flash from space  
790 and the ground, *Earth and Space Science*, <https://doi.org/10.1029/2020EA001249>.  
791

792 Warren, S. G. (1984). Optical constants of ice from the ultraviolet to the microwave. *Appl. Opt.*, 23, 1206-  
793 1225.  
794

795 Warren, S. G., and Brandt, R. E. (2008). Optical constants of ice from the ultraviolet to the microwave: A  
796 revised compilation. *Journal of Geophysical Research*, 113, D14220.  
797 <https://doi.org/10.1029/2007JD009744>  
798

799 Yang, J., Zhang, Z., Wei, C., Lu, F., and Guo, Q. (2017). Introducing the new generation of Chinese  
800 Geostationary Weather Satellites, Fengyun-4. *Bulletin of the American Meteorological Society*, 98(8),  
801 1637– 1658. <https://doi.org/10.1175/BAMS-D-16-0065.1>  
802

803 Yuter, S. E., and Houze Jr., R. A. (1995). Three-dimensional kinematic and microphysical evolution of  
804 Florida cumulonimbus. Part II: frequency distributions of vertical velocity, reflectivity, and differential  
805 reflectivity. *Mon. Wea. Rev.*, 123, 1941-1963.  
806

807 Zhang, D., and Cummins, K. L. (2020). Time evolution of satellite-based optical properties in lightning  
808 flashes, and its impact on GLM flash detection. *Journal of Geophysical Research: Atmospheres*, 125.  
809 Special Section: A New Era of Lightning Observations from Space. doi: 10.1029/2019JD032024.

810

811

812

813

814

815

816

817

818

819

820

821

822

823

824

825

826

827

828

829

830

831

832

833

834

835

836

837

838

839

840

841 **Figure Captions and Tables**

842

843 **Figure 1.** **a)** GOES-16 infrared satellite image overlaid with LMA sources. **b)** Maximum  
844 reflectivity  $Z_{\max}$  and LMA sources. White filled circles correspond to LMA sources before  
845 ASIM video frame 1 and after frame 4. Black filled squares are LMA sources in the field  
846 of view of MMIA. The white squares and the numbers indicate the five analyzed areas of  
847 interest (boxes). **c)** Composition of 777.4 nm (red) MMIA camera stacked frames with  
848 the indication of the five considered areas, LMA sources **d** and the markers (letters) are  
849 used to identify the leaders during the period of the video frames. LINET Cloud-to-ground  
850 strokes: negative ( $\times$ ), positive (+).

851

852 **Figure 2.** LMA data of the flash on 22 November 2018 at 08:57:21.4413 UT. The top  
853 panel is altitude of LMA sources versus time (seconds); the left panel is a plan view map;  
854 the panels at the right show altitude (km) by latitude and longitude. LMA sources are  
855 colored by time. Markers *a* to *k* are used as reference in the text. LINET cloud-to-ground  
856 strokes (red symbols:  $\times$  negative, + positive). The exposure times of the four MMIA video  
857 frames are indicated as well the part of the field of view (FOV) of MMIA.

858

859 **Figure 3.** **a)** LMA; **b)** ASIM 337/4 nm (blue) and 777.3/5 nm (red) including the reference  
860 markers (letters); **c)** 2 ms-integrated radiances of GLM (black) and ISS-LIS (red); **d)**  
861 MMIA 180-230 nm (UV) photometer; **e)** Magnetic field measured at the UPC's Cape  
862 Verde ELF station. Vertical lines indicate the times of the MMIA video frames 1-4.

863

864 **Figure 4.** Consecutive MMIA camera frames in blue (337.0/4 nm) (left column) and red  
865 (777.4/5 nm) (right column) channels. LMA sources (white dots) are overlaid in each  
866 image. Locations of GLM events (grey squares) are plotted in the MMIA red images.  
867 GLM radiances (grey) at each location are integrated for the time of the frame.

868

869 **Figure 5.** Reflectivity contoured-frequency-by-altitude diagram (CFAD). **a)** Box 1:  
870 location of the CG strokes; **b)** Box 2: central leader channel emerging from the location  
871 of the CG towards east; **c)** Box 3: southeast leader branch; **d)** Box 4 north leader branch;  
872 **e)** Box 5: northeast leader branch. Horizontal heavy dashed line indicates the altitude of  
873 the leader sources in each box. Solid line marks the 50<sup>th</sup> percentile of the reflectivity  $Z$   
874 and the dashed line the 90<sup>th</sup> percentile

875

876 **Figure 6.** Average radiance of the blue (337.0 nm) and red (777.4 nm) from video  
877 frames for the boxes 1 to 5. Dot-dash line indicates the altitude of the leader in each  
878 box. Solid line corresponds to the 20 dBZ radar echo top.

879

880 **Table 1.** Relative optical depth of the cloud section above the lightning leader channels  
881 up to 10 km. Optical depths are relative to Box 1.

Relative optical depth	
Box 1	1
Box 2	0.5
Box 3	2
Box 4	0.9
Box 5	0.9

882

883

884

885

886

887

888

889

890

891

892

893

894

895

896

897

898

899

900

901

902

903 **Appendix**

904

905 *Heymsfield et al.* (2002 and 2013) have presented assimilation of experimental data to  
906 provide ice particle size distributions. One of the common functional forms of the particle  
907 size distribution  $N(D)$  is the gamma function:

908

$$909 \quad N(D) = N_{o\Gamma} D^\mu e^{-\lambda_\Gamma T} \quad (cm^{-4})$$

910

911 Where  $D$  is the particle diameter,  $N_{o\Gamma}$  is the intercept,  $\lambda_\Gamma$  is the slope, and  $\mu$  is the shape.  
912 The last three parameters are derived from radar and temperature variables as presented  
913 by *Heymsfield et al.* (2002). The simplified equation for the intercept:

914

$$915 \quad N_{o\Gamma} = \frac{Z \lambda_\Gamma^{(5.5+\mu)}}{1.2 \cdot 10^8 \Gamma(5.5 + \mu)}$$

916

917 Where  $Z$  is the radar reflectivity factor ( $mm^6 m^{-3}$ ) converted from observed weather  
918 radar measuring in dBZ. Taking into account the use of a C-Band weather radar and  
919 measurements above the 0 °C,  $Z$  can be expressed as (*Heymsfield et al.*, 2002):

920

$$921 \quad Z = 10^{\left(\frac{dBZ+7.2}{10}\right)}$$

922

923 where, 7.2 dBZ is to correct the ice/water dielectric constant effect. To simplify, we adopt  
924 the median dBZ reflectivity at each level shown in Figure 5. The slope  $\lambda_\Gamma$  and the shape  
925  $\mu$  are estimated from the median fitted functions in *Heymsfield et al.*, (2002), respectively:

926

$$927 \quad \lambda_\Gamma = 24 e^{-0.049T} \quad (cm^{-1})$$

928

$$\mu = 0.13 \lambda_\Gamma^{0.64} - 2$$

929

930 Where  $T$  is the temperature in °C. The maximum diameter for each distribution is  
931 calculated according to the region of the cloud. For Box 1 and 5 the maximum diameter  
932 is selected for convective type (*Heymsfield et al.*, 2013):

933

$$934 \quad D_{max} = 2.1 e^{0.070T} \quad (cm)$$

935

936 Whereas for the stratiform areas in Box 2, Box 3 and Box 5:

937

938 
$$D_{max} = 1.1 e^{0.069T} \text{ (cm)}$$

939

940 In the lower part of the distribution  $D$  has been limited to 20  $\mu\text{m}$ . Once the fitted gamma  
941 functions  $N(D)$  are obtained, photon mean free paths are calculated according to  
942 *Thomason and Krider (1982)*:

943

944 
$$\Lambda \approx \frac{1}{\int_{D_{min}}^{D_{max}} \pi D^2 N(D) dD}$$

945

946 Finally, the optical depth  $\tau$  is calculated according to the corresponding geometric  
947 deepness  $L$  of the given reflectivity region above the lightning channel:

948

949 
$$\tau = \frac{L}{\Lambda}$$

950

951 With the available data and the presented calculations, we cannot provide a precise  
952 estimation of the optical depth. From our experience some of the aspects to consider in  
953 the future are:

954

955 1) Better radar vertical resolution is convenient. Here we cannot resolve levels higher  
956 than 10 km for all the regions of the flash, because the radar has been configured  
957 to monitor rain mainly.

958 2) By increasing the number of elevations or scanning continuous vertical cross  
959 sections (like sector range height indicator – RHI) with a polarimetric radar, like  
960 this one, polarimetric variables like differential radar reflectivity (ZDR), specific  
961 differential phase ( $K_{DP}$ ) and correlation coefficient among horizontal and vertical  
962 polarization can be augmented to estimate the type of ice particles and its size (*Liu  
963 and Chandrasekar, 2000*);

964 3) C-band radars detect mostly precipitation size particles. The referenced works  
965 allow to extend to lower size particles, even to the few  $\mu\text{m}$  size. However, we  
966 have found that at temperatures lower than  $-40 \text{ }^\circ\text{C}$  ( $\sim 11 \text{ km}$ ) the density of low

967 sized particles increases several orders of magnitude providing very dense clouds  
968 that result in an increase of the optical depth by an order of magnitude. A similar  
969 unrealistic effect is found by *Rutledge et al.* (2020) in relation of the temperature  
970 dependence of the intercept parameter.

971

972 Despite the assumptions and limitations, the relative optical depths presented in Table 1  
973 present a reasonable agreement with the observed luminosity features in each box.

974

975

976

977

978

979

980

981

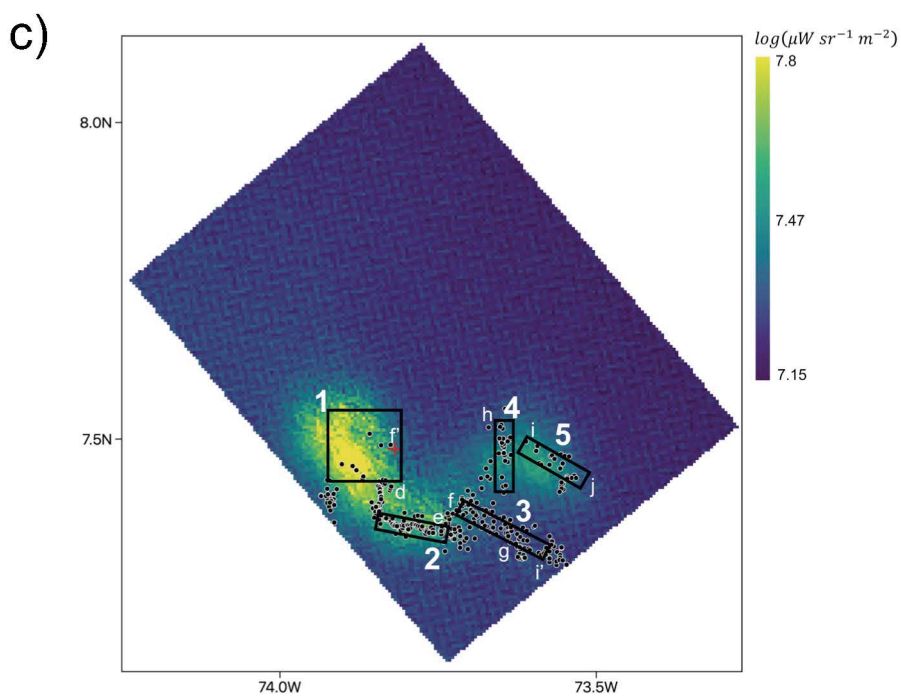
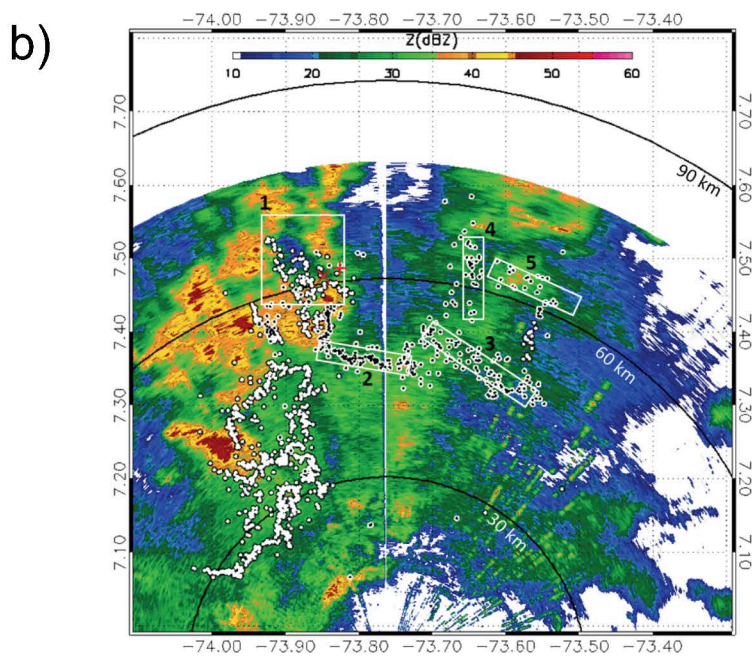
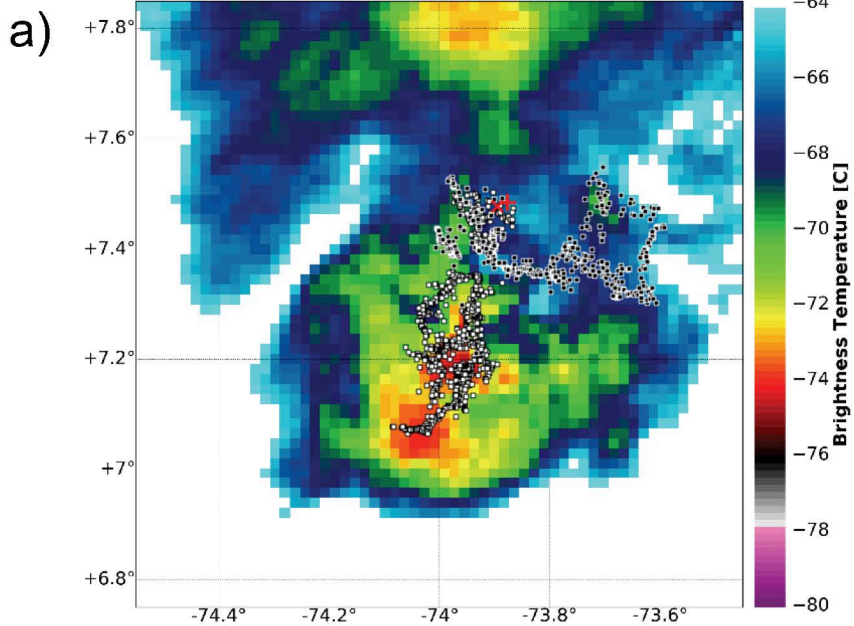
982

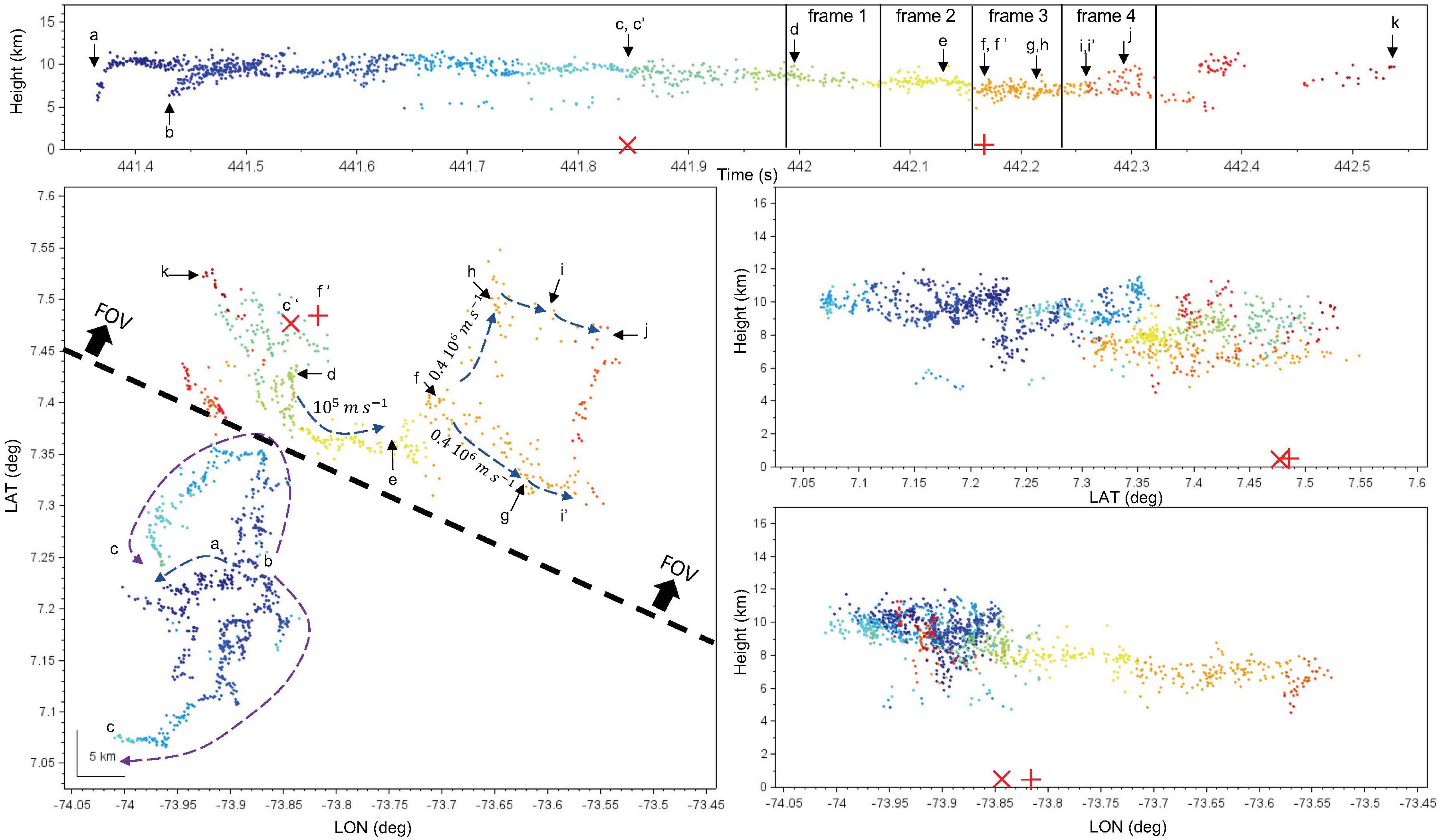
983

984

985

Figure 1





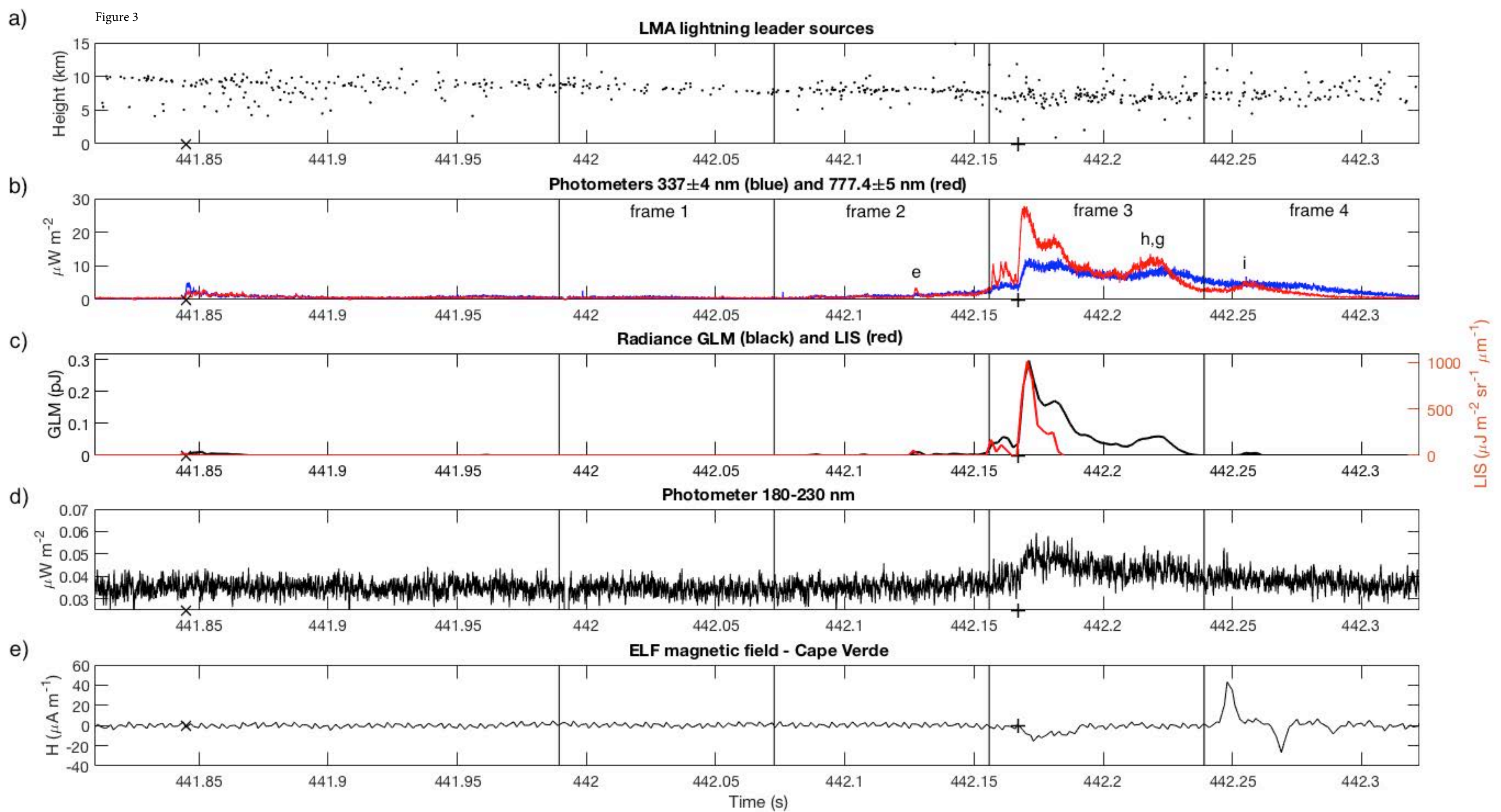


Figure 4

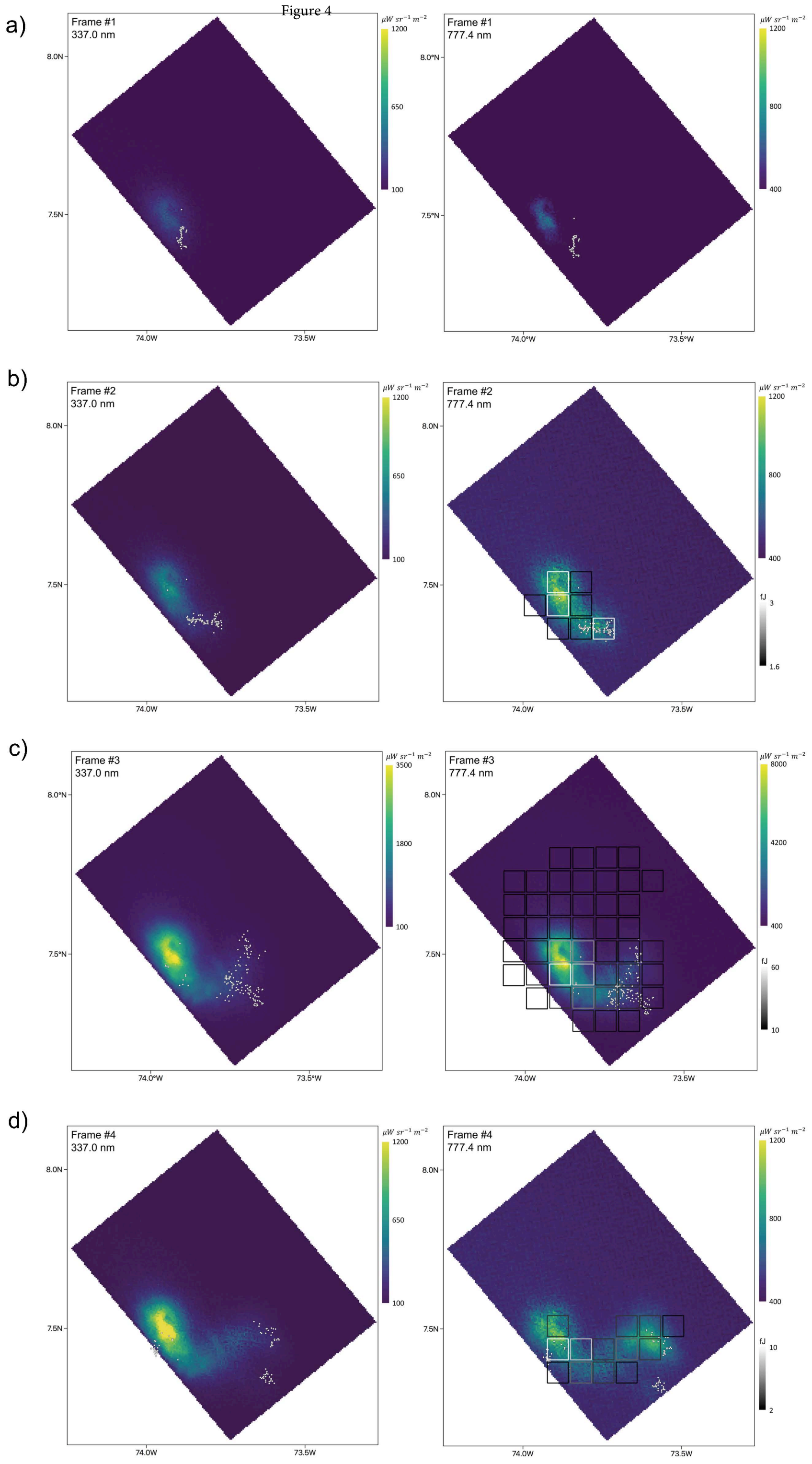


Figure 5

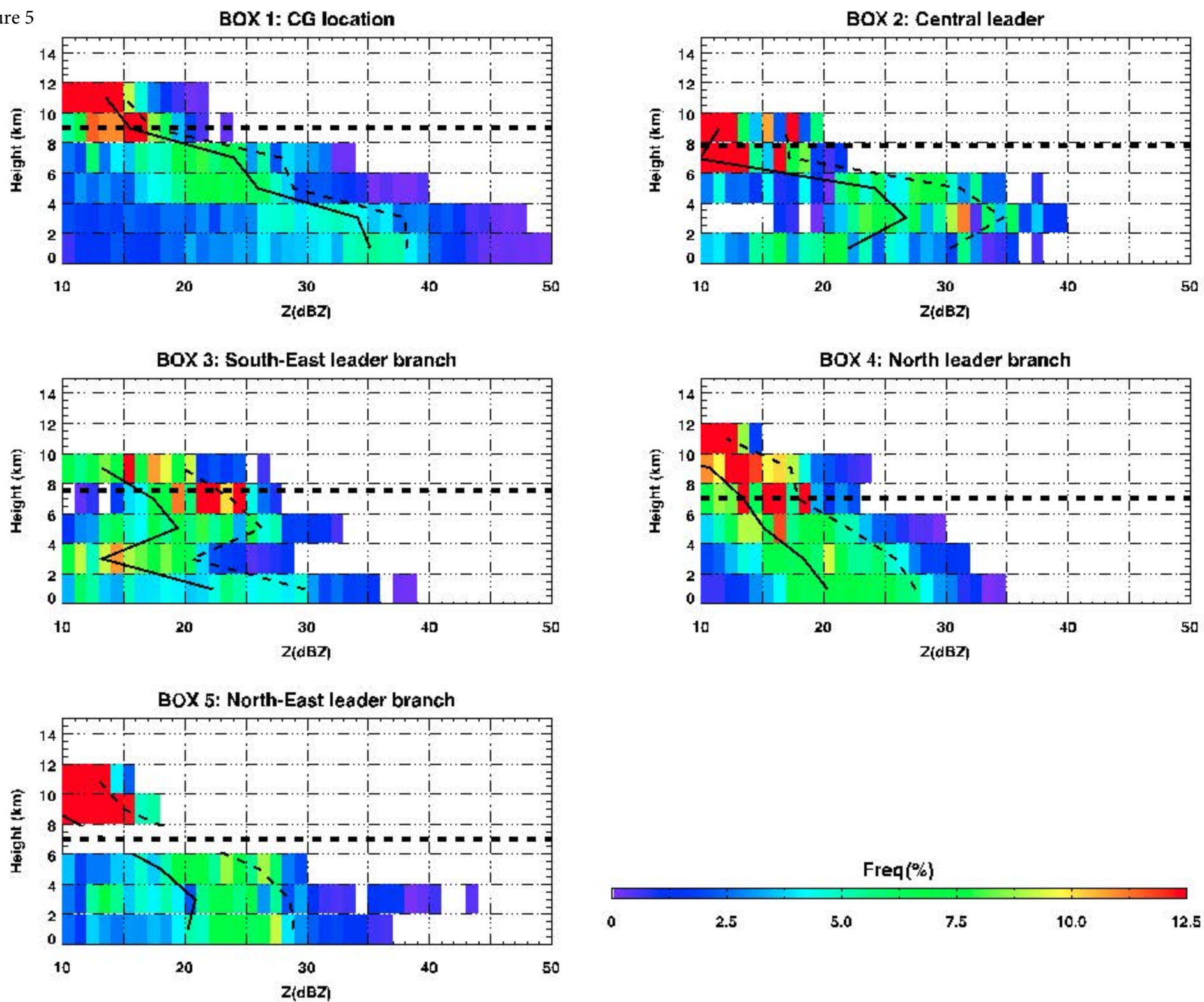


Figure 6

